Study of Cr_2O_3 nanoparticles supported on carbonaceous materials as catalysts for O_2 reduction reaction

Paloma Almodóvar [a], Florencio Santos [b], Joaquín González [c,*], Julio Ramírez-Castellanos [d], José María González-Calbet [d], Carlos Díaz-Guerra [a], Antonio J. Fernández Romero [b,*]

[a] Departamento de Física de Materiales, Facultad de Ciencias Físicas, Universidad Complutense de Madrid, Ciudad Universitaria s/n, 28040 Madrid, Spain
[b] Grupo de Materiales Avanzados para la Producción y Almacenamiento de Energía, Universidad Politécnica de Cartagena, Aulario II, Campus de Alfonso XIII, 30203 Cartagena, Spain
[c] Departamento de Química Física, Facultad de Química, Regional Campus of International Excellence "Campus Mare Nostrum", Universidad de Murcia, 30100 Murcia, Spain
[d] Departamento de Química Inorgánica, Facultad de Ciencias Químicas, Universidad Complutense de Madrid, Ciudad Universitaria s/n, 28040 Madrid, Spain

ARTICLE INFO

ABSTRACT

A series of chromium oxides (Cr_2O_3) nanoparticles supported on different carbonaceous material, namely: graphene, graphene oxide (GO) and graphite, were synthetized by precipitation of the salt precursors with precipitant (ammonia) and the subsequent thermal treatment. The catalytic activity of these composites and the Cr_2O_3 nanoparticles have been analysed by Koutecky-Levich (KL) and rotating ring-disc electrode methods and the results have been discussed following a model proposed here, which considers the O_2 electrosorption as the rate determining step. Among them, graphite and graphene based composites have better catalytic activities and their behaviours agree with the proposed treatment: logarithm dependent of the intercept and non-dependent slopes values of the KL plots with the potential. Cr_2O_3-graphite shows a mechanism interchanging 4 e-, which has been attributed to a graphite- Cr_2O_3 nanoparticles interaction. Besides, Cr_2O_3-graphite-based electrodes have been tested as cathode in a Zn/PVA-KOH/air battery, confirming its good properties to be applied as positive electrode in metal-air batteries.

1. Introduction

Sustainable energy storage and conversion has become the key issue for the new energy distribution grids and consequently, has attracted much attention from research groups and industry. In this sense, fuel cells and rechargeable metal-air batteries are next-generation to be energy devices for clean power. These devices rely in the even prosaic and overworked, but still in the spotlight, oxygen reduction reaction (ORR).

The sluggish kinetics of oxygen reduction reaction [1] (ORR) is the decisive factor in such devices. Despite tremendous efforts have been made, developing oxygen reduction catalysts with high activity and low cost still remains a great challenge for scientists. Researchers have struggled for decades to find efficient, stable catalysts to speed up the kinetics and to minimize energy losses, but so far catalytic efficiency and long term stability best results are obtained with high ratios of noble metals such those belonging to the PGM group (platinum group metals) as Pt, Pd or Ru. However, the cost of a catalyst from the Pt group for massive implementation is prohibitive being the most expen-

sive metals together with gold. Apart from price, the European Commission has considered the PGM group metals as critical material in his first report in 2011[2]. Thus, several approaches have been explored to replace or reduce the use of noble metal as catalyst for ORR.

Alloying platinum with transition metals, such as Mn, Fe, Ni, Co, Mo and Cu[3,4] or combining nonmetallic elements, such as B, P, S, and N embedded in a carbon-based matrix (heteroatom doped carbons)[5,6], pre-treating carbon materials in order to introduce functional groups or defects[7] or using macrocyclic transition metal complexes[8,9] are one of the explored most promising alternatives.

Carbon materials have been subjected to extensive research during the last decade, since they are considered as a promising new class of catalysts for ORR to replace the PGM group metals, firstly reported by Dai's group in 2009 [10]. Among them, graphene-based materials are expected to play a significant role. However, pristine graphene is not a good catalyst for ORR due to its zero band gap and the absence of active sites (i.e. low coordinated sites that are generally containing functional groups) [11,12].

It has to be noted that the nomenclature of graphene-based materials used in the literature is clearly inconsistent in several articles and the term of graphene has been used to encompass a wide range of derivate materials [13]. Firstly, graphene-based catalyst term is frequently used to materials containing graphene, graphene oxide, reduced graphene oxide, and so on. In addition, a differentiation must be made between functionalized graphene, including groups covalently bonded to its surface, and doped graphene, where heteroatoms, metal oxides, etc. are incorporated into the carbon lattice.

Furthermore, graphene and other carbon materials have been modified incorporating heteroatoms or transition metal oxides to improve the catalyst properties. It has been demonstrated that carbon nanomaterials such as carbon nanotubes (CNTs,1D) and graphene (2D) doped by different heteroatoms (for example, N, B, P, S, Br, Cl, and I) exhibit high ORR, but even undoped carbon materials adsorbed with polyelectrolytes can show good ORR catalytic activities[14].

Several graphene-based materials have been reviewed recently (see [11,13,14]). Heteroatom doping can modify the electronic structures and surface chemical properties of graphene and other carbon networks, facilitating the electrochemical reaction on the carbon surface. Studies on a wide variety of materials have been reported, including B, N,S-doped CNTs[15], N,B-doped graphene [16], N,S-doped graphene [17], N,S-doped reduced graphene oxide (rGO) [18], P-doped graphite layers [19], etc.

Besides, different transition metal oxides exhibited activity toward the ORR and were proposed as one of the choices to substitute noble metal catalysts in alkaline solution[20–23]. However, metal oxides usually show low conductivity values, which inhibits its application in electrochemical research fields. In order to overcome this shortcoming, these oxides are frequently supported on carbon materials, which improve their conductivity properties. Graphene has been frequently used to support different metal oxides, because it acts as electron carrier for highly-efficient electronic exchange between graphene and the metal oxides, which has shown great promise for ORR [24]. Also, chromium oxide has been supported on reduced graphene oxide and its catalyst activity for ORR was demonstrated in alkaline medium[25].

In this work, chromium oxide nanoparticles have been synthesized and supported on different carbonaceous materials, such as graphite, graphene and graphene oxide (GO). These nanocomposites have been characterized by various experimental techniques and their catalyst activity towards the ORR reaction in alkaline medium have been analysed by rotating ring-disk electrode (RRDE) technique. All carbon-based Cr_2O_3 nanocomposites showed better catalytic properties than Cr_2O_3 nanoparticles alone, confirming that carbonaceous support greatly improves the catalyst process. However, only the graphite-based nanocomposite revealed a quasi-pure 4 e$^-$ ORR conversion, which was explained as due to a synergetic activity of graphite and Cr_2O_3, on the basis of a graphite-Cr_2O_3 interaction that enhances the catalyst behaviour. Besides, the results are in agreement with a ORR mechanism where the rate determining step has been described by an electrosorption/desorption step.

Finally, Cr_2O_3-graphite based cathodes have been tested in Zn/PVA-KOH/air batteries, which can be considered as alternative to lithium-ion[26], confirming their application in storage energy devices.

2. Material and methods

2.1. Chemicals

All chemicals used in the experiments are analytic reagent grade. Chromium sulphate, $Cr_2(SO4)_3 \cdot 12H_2O$ was purchased from Merck, India. Ammonium hydroxide (liquor ammonia) was purchased from SRL while graphene (graphene nanoplatelets 99%) was purchased from Strem Chemicals. Deionized water was used throughout the experiment.
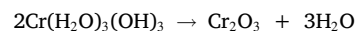
2.2. Synthesis methods

2.2.1. Synthesis of Cr_2O_3 nanoparticles.

The synthesis of chromium oxide (Cr_2O_3) nanoparticles was carried out by the precipitation of chromium hydroxide ($Cr(OH)_3$) according to the reaction[27,28]:

$$Cr(NO_3)_3 9H_2O \; + \; NH_4OH \; \rightarrow \; 3NH_4NO_3 \; + \; Cr(H_2O)_3(OH)_3 \; + \; 6H_2O$$
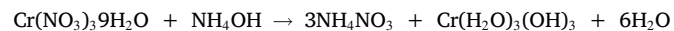
For the precipitation of chromium hydroxide, aliquots of ammonia were added until reaching a pH ≈ 10 with constant stirring and controlled temperature of 60 °C. The obtained product was rinsed, washed with distilled water, dried, grinded and finally annealed in air at 350 °C for 3 h in order to get the Cr_2O_3 nanoparticles according to the following reaction:

$$2Cr(H_2O)_3(OH)_3 \; \rightarrow \; Cr_2O_3 \; + \; 3H_2O$$

2.2.2. Synthesis of GO

Graphene oxide (GO) was prepared following a typical procedure by using a modified Hummers method [29]. Synthesis started with the preparation of 70 ml of sulphuric acid (H_2SO_4, 95–98%, Sigma-Aldrich) and 1.5 g of sodium nitrate ($NaNO_3$, Merk, 99.5%) solution. After that, 2 g of graphene were added under vigorous magnetic stirring. To reach the desire compound, 9 g of potassium permanganate ($KMnO_4$, Aldrich Chemical, 99%) were slowly added into the solution. The resulting solution was stirred until it turned to a dark green colour where the whole oxidation reaction was completed. To stabilize and exfoliate the graphene oxide and eliminate the excess of $KMnO_4$, several solutions composed by H_2SO_4, hydrogen peroxide (H_2O_2 30%, Labkem) and distilled water were added. The resulting product was collected by centrifugation for 20–30 min until pH 7 was reached. Afterwards, the final product was preserved in water solution.

2.2.3. Synthesis of Cr_2O_3 nanocomposites.

Graphite flakes (Alfa Aesar, 99.8%), graphene nanoplatelets (Strem Chemicals, 99%) and GO were added to the above-mentioned initial solution in order to obtain a Cr_2O_3/carbon compound 1:1 M ratio. To obtain the composites, the synthesis route was adapted to add the allotropic forms of carbon during the formation of the nanoparticles. Basically, the carbon allotrope and the salt precursor were added in the reaction pot simultaneously. The aim of such procedure was to get the nanoparticles precipitation onto the allotropes flakes. In addition, this mild new route did not alter the composition and structure of the final nanoparticles and would allow us to obtain a most uniform distribution of all components.

To obtain Cr_2O_3-GO nanocomposite the allotrope had to be added at a later stage, after synthesis of the Cr_2O_3 nanoparticles, as it has been observed that when a GO solution is added to a solution that contains Cr^{3+} cations, these are spontaneously adsorbed by GO [30,31]. This causes the reduction of GO, creating bonds of its functional groups with Cr^{3+} and also producing an uncontrolled precipitation of a mixture of different phases of chromium oxides and hydroxides. To avoid this drawback, the GO solution was added once the precursor salt has precipitated, keeping constant stirring for 12 h at 80 °C. In this way, the nanoparticles re-aggregate among themselves (flocculate) and are deposited on the GO sheets. The final thermal treatment to obtain Cr_2O_3-GO was kept as in the case of normal precipitation, 350 °C for 2 h.

2.3. Structural characterization.

The structure of the as-grown samples was assessed by x-ray diffraction (XRD) on a Philips X'Pert PRO diffractometer using Cu Kα radiation. Micro-Raman measurements were carried out at room temperature in a Horiba Jovin-Ybon LabRAM HR800 system. The samples were excited by a 633 nm He-Ne laser on an Olympus BX 41 confocal microscope with a 100x objective. A charge coupled device detector was used to collect the scattered light. The spectral resolution of the system used was ∼ 1 cm^{-1}. Laser power density was carefully adjusted in order to avoid heating or irradiation effects. Spectra shown in this work were taken under the same experimental conditions. High resolution transmission electron microscopy (HRTEM) images were obtained in a field emission Jeol JEM 3000F microscope operating at 300 kV. For HRTEM observations, nanoparticles were dispersed in a butanol solution. Drops of this solution were then deposited onto amorphous carbon-coated copper grids.

2.4. Electrochemical characterization.

The electro-chemical performance tests were conducted by using a Biologic VSP Modular 5 channels potentiostat/galvanostat electrochemical workstation coupled with a rotating disk-ring electrode system RRDE-3A (Als Co.Ltd.) with a three-electrode system consisting of a (glassy carbon) GC disk-Pt-ring as working electrode, a Pt wire as counter electrode and an Ag/AgCl reference electrode. To address the influence of a possible Pt dissolution and re-deposition on the active material during the measurements, we carried out the same experiments using a stainless steel counter electrode. The obtained results agreed with those obtained using Pt as counter electrode. Based on this agreement between the curves obtained for different counter electrodes, we can discard the Pt dissolution under testing and its influence on the results obtained for the catalytic activity of our Cr_2O_3-based materials. The working electrodes were prepared as follows. Catalyst dispersions were prepared by mixing 15 mg of the catalyst powder in 2 ml of Nafion solution (9 ml IPA + 1 ml Nafion 5%) followed by 30 min ultrasonication. The glassy carbon disk electrodes (4 mm diameter, 0.1256 cm^2 surface area) served as the substrate and were polished to a mirror surface using different alumina grades. 5 μl of the prepared catalyst suspension was pipetted onto the glassy carbon disk electrodes and then fully dried. The loading of Cr_2O_3 based composites or nanoparticles on the electrode was 0.3 mg/cm^2. The working electrode was first cycled between 0.2 and −1V vs. Ag/AgCl at a scan rate of 50 mVs^{-1} in a N_2-saturated (30 min) 0.1 M KOH solution at room temperature until reproducible cyclic voltammetry (CV) results were obtained. Then, the measurements of oxygen reduction were conducted by linear sweep voltammetry (LSV) between 0.2 and −1 V vs. Ag/AgCl in air saturated (30 min) 0.1 M KOH electrolyte with a scan rate of 50 mVs^{-1}.

Cr_2O_3-graphite composite was tested as cathode electrode in a Zn/PVA-KOH/air battery, with Zn powder as negative electrode and a PVA-KOH gel polymer as the electrolyte. The contact area was always 1.1 cm^2 and nickel mesh current collectors were used. Zn powder (purity 98.5%) was supplied by Goodfellow and an amount of 0.5 gr was used in the negative electrode. PVA-KOH gel polymer electrolytes were synthesized as it was described previously[26,32,33] and conductivity values of 0.34 Scm^{-1} at 20 °C were obtained for these. PVA MOWIOL 18–88 (MW 130.000 and KOH (85%) were obtained from Sigma-Aldrich. Besides, MilliporeTM water with resistivity of > 18 MΩcm was always used.

Cathodes for Galvanostatic discharges and polarizations tests were 25 wt% of Cr_2O_3-composites or Cr_2O_3 nanoparticles, 5% PVdF and the rest carbon black. Total weight of the cathodes was 0.105 ± 0.001 g. Galvanostatic Discharges at −5 mA and polarization analysis were performed using the same Biologic potentiostat/galvanostat.

3. Results and discussion

3.1. Structural characterization of Cr_2O_3 and its composites

3.1.1. XRD

The long-range structural order and phase purity of the obtained samples were assessed by powder X-ray diffraction (XRD). The corresponding patterns (Fig. 1) are in perfect agreement with those of Cr_2O_3 (JCPDS file 96–901-2231, lattice constants $a = b = 4.958$ Å, $c = 13.593$ Å, space group R-$3c$). The diffraction maximum appearing at 26.55° in XRD patterns from the composites with graphite and graphene corresponds to C (0 0 2). No carbon-related maxima were found in XRD patterns of the GO composite, probably due to its low crystallinity. Diffraction maxima corresponding to secondary phases or unreacted precursors were not observed in our XRD measurements. Scherrer analysis of the Cr_2O_3 related maxima reveal little difference in the crystallite size among the different samples, which ranges between 21.3 nm (Cr_2O_3-graphite composites) and 23.5 nm (Cr_2O_3-GO samples).

3.1.2. Raman

The short range structural order of the Cr_2O_3 nanoparticles and their composites was investigated by micro-Raman spectroscopy. Fig. 2a shows a representative example of the chromium oxide spectrum, with peaks centred at 300 cm^{-1} (E_g symmetry), 355 cm^{-1} (E_g), 527 cm^{-1} (E_g), 555 cm^{-1} (A_{1g}) and 615 cm^{-1} (E_g), which are all characteristic of Cr_2O_3[34]. Another broad, dominant peak can be observed centred at about 835 cm^{-1}. This peak has been rarely reported in the literature and its origin is unclear. We tentatively attribute this band to a O-Cr^{3+}-O vibration associated to surface structural disorder[35], in agreement with the small size of our nanoparticles obtained at 350 ^{0}C. In fact, we have found that the relative intensity of this Raman peak decreases upon annealing the sample up to 700 °C. Raman spectra of the composites (Fig. 2b) show, besides the Cr_2O_3 related peaks, bands centred at 1332 cm^{-1} (D band), (1581 – 1586) cm^{-1} (G), 1614 cm^{-1} (D'), 2675 cm^{-1} (2D), and 2917 cm^{-1} (D + D'). The D peak is a defect-activated band associated to the breathing modes of six-atom rings K-point phonons (A_{1g} symmetry). The D' band is also related to defects, since it originates from intravalley one-phonon double resonance Raman processes involving one longitudinal optical phonon near the Γ point of the Brillouin zone (BZ)
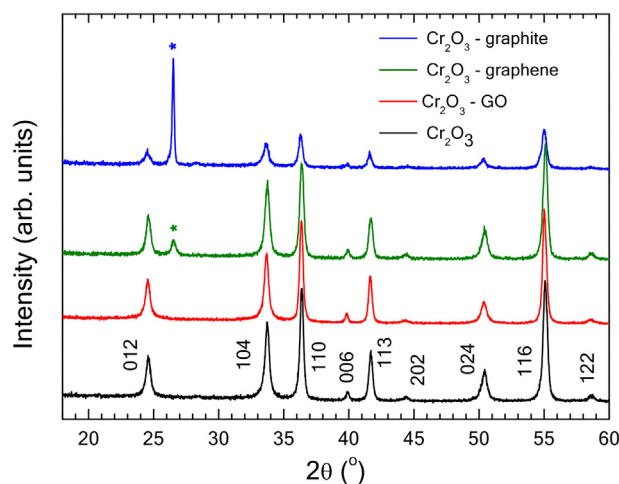

Fig. 1. XRD patterns of the Cr_2O_3 nanoparticles and their composites with graphite, graphene and GO. Only the main diffraction maxima of Cr_2O_3 have been labelled. Peaks at 26.55° marked with an asterisk correspond to C (0 0 2) from graphite and graphene.
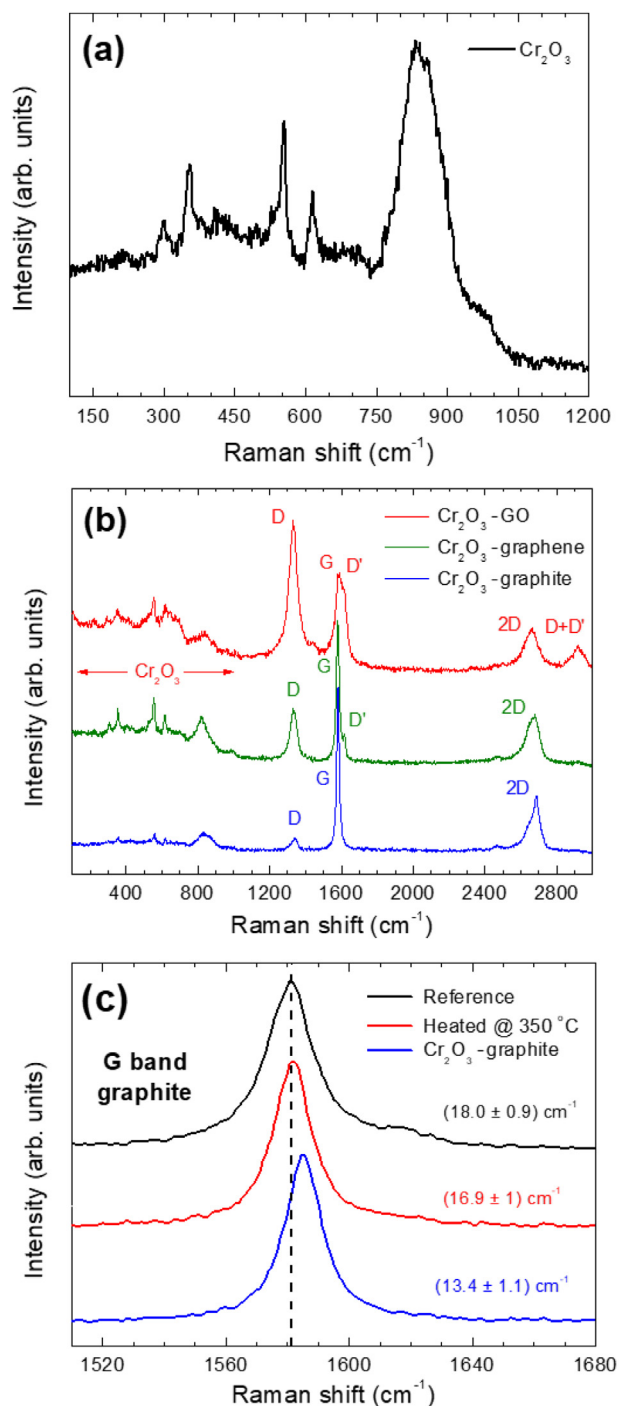
Fig. 2. Raman spectra of Cr_2O_3 nanoparticles obtained at 350 °C (a) and their composites with graphite, graphene and GO (b). (c) Detail of the G band observed in Raman spectra of pristine graphite, graphite annealed at 350 °C and a Cr_2O_3-graphite composite. FWHM of each band is indicated above the corresponding spectrum.

and one defect. The G band is a doubly degenerate phonon mode (E_{2g} symmetry) at the BZ center that is due to the bond stretching vibrations of all pairs of sp^2 atoms in both rings and chains of carbon networks [36,37]. 2D band corresponds to the harmonic (second order Raman scattering) of an in-plane transverse optical (TO) mode close to the zone boundary K point [38]. The higher intensity of the D' and D + D' peaks in the GO composite indicate a higher structural disorder in this sample, in agreement with our XRD data. In addition, a clear shift of the G band towards higher wavenumbers was observed

in the graphite composite. In fact, measurements carried out in different spots of the same composite, as well as in different samples, show that while this band appears centered at (1581.0 ± 0.5) cm^{-1} in the samples containing graphene and GO, it is peaked at (1585 ± 1) cm^{-1} in the Cr_2O_3-graphite composite. In principle, such shift could be attributed to a compressive strain, which has been reported to be sometimes induced in carbon materials upon annealing [39]. Such strain does not make the full width at half maximum (FWHM) of the G band to decrease; on the contrary, it is found to be sometimes increased due to an enhancement of the closely positioned D' band [40]. In order to clarify this point, we measured Raman spectra of the same graphite used to synthesize the composites before and after annealing two hours at 350 °C, which is the same thermal treatment used to obtain the corresponding composites with Cr_2O_3 nanoparticles. Results are shown in Fig. 2c. While spectra of the pristine and annealed graphite samples show the G band peaked at 1581 cm^{-1}, that of the composite shows that band peaked at 1585 cm^{-1}. Most importantly, this signal can be very well fitted with a single Lorentzian profile and the corresponding FWHM is significantly smaller in the case of the Cr_2O_3-graphite composite. Indeed, spectra taken in the same experimental conditions in at least ten spots of two different samples of each kind reveal that the FWHM of the G band is (18.0 ± 0.9) cm^{-1} for as-received graphite, (16.9 ± 1.0) cm^{-1} for annealed graphite and just (13.4 ± 1.1) cm^{-1} for Cr_2O_3-graphite composites. These observations seem to rule out strain and point towards electron doping as a possible mechanism responsible for the G band shift and decreased FWHM [40,41] and evidence a strong interaction between chromia nanoparticles and graphite in our composites. This process has been mainly investigated in Raman spectra of graphene, although the origin of the G band is the same in both materials. Furthermore, recent density functional theory (DFT) calculations and Raman measurements [42] reveal an interfacial charge transfer from graphene to chromia and even how chromia is able to induce a significant carrier spin polarization in the graphene layer. Although further studies are necessary to fully understand the reasons behind this charge transfer process, the formation of Cr-C bonds can be in principle ruled out as the origin of such interaction, since the formation of Cr carbides was neither detected by XRD nor by micro-Raman measurements.

3.1.3. TEM

Low magnification TEM images (Fig. 3a) show thin nanoplates of nearly hexagonal shape and sizes ranging between 10 and 70 nm, approximately. HRTEM images, like that shown in Fig. 3b, reveal the crystalline nature of the obtained material. The fringe spacing marked in the image measures 2.49 Å, which corresponds to the $(1 1 0)$ interplanar spacing of Cr_2O_3. The average diameter of the nanoparticles is (33 ± 14) nm and the particle size follows a lognormal distribution (Fig. 3c). The morphology and crystallinity of the oxide nanoparticles is preserved in all the composites, where they appear quite uniformly distributed on the graphite, graphene and GO layers. An example is shown in Fig. 3d, corresponding to the Cr_2O_3-graphene sample. The inset shows the stacking of several layers of the carbon compound. Fig. 3e shows a HRTEM image of a Cr_2O_3 nanoparticle of the graphite-containing composite, while Fig. 3f shows the area marked in the previous figure at higher magnification. The fringe spacings indicated in the image measure 2.65 Å and 3.58 Å, which respectively correspond to the $(1 0 4)$ and $(0 1 2)$ interplanar spacings of Cr_2O_3.

3.2. ORR activity of Cr_2O_3 and its composites.

Fig. 4 displays the RRDE LSV curves of the different chromium oxide–carbon composites (4b: Cr_2O_3-GO; 4c: Cr_2O_3-graphene; 4d: Cr_2O_3-graphite), as well as those obtained from the nanoparticles without carbon allotropes (Fig. 4a). The LSV curves have been recorded at
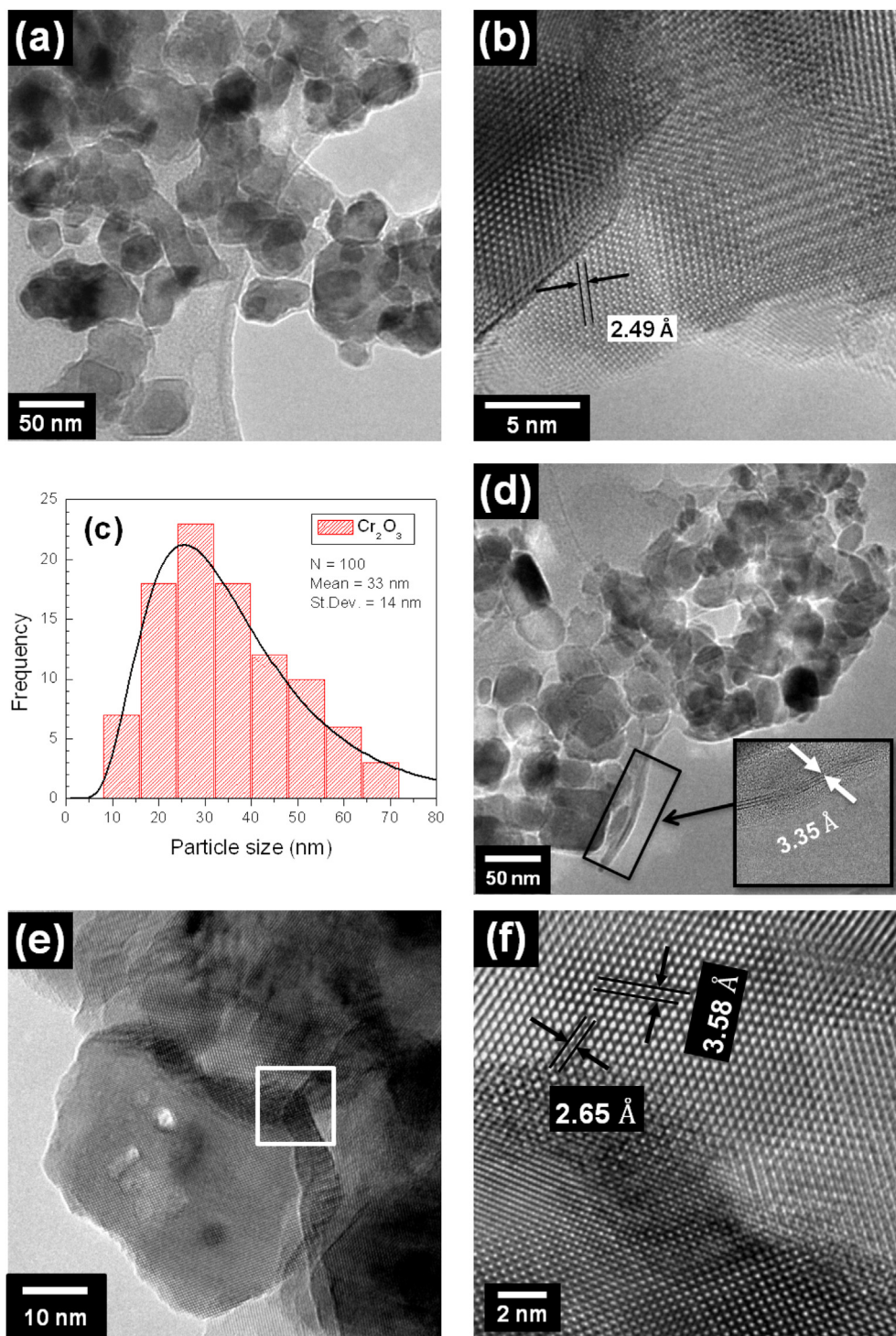
Fig. 3. (a) Low magnification TEM image of the investigated Cr_2O_3 nanoparticles. (b) HRTEM micrograph showing the crystalline nature of the obtained oxide. (c) Cr_2O_3 particle size distribution histogram and lognormal fitting. (d) Low magnification TEM image of the Cr_2O_3-graphene composite showing the oxide nanoparticles distributed on the carbon layers. Stacked carbon layers can be observed in the inset. (e) HRTEM micrograph of a chromia nanoparticle in the Cr_2O_3-graphite sample. (f) HRTEM image of the area marked in Fig. 3 (e).

0.05 Vs^{-1} scan rate in air and N_2 saturated 0.1 M KOH electrolyte at different rotation rates.

From the curves in this figure it can be seen that there is no peak in the N_2 saturated electrolyte, a fact that means that the catalysts were apparently stable in the alkaline electrolyte. When the air-saturated electrolyte is considered, a cathodic current plateau is observed at the disk electrode for potentials between -0.6 V and -1.0 V. This can be attributed to the catalytic performance of the materials laid

in the disk electrode for oxygen reduction reaction. It can be also observed that the disk current intensity increased with increasing rotation speed at the same potential, indicating a convective mass transport influence that could be analysed in terms of a Koutecky-Levich (KL) type equation (see below).

When comparing the performance of the different composites at a given rotation rate, it can be concluded similar ability of Cr_2O_3-graphene and graphite modified electrodes, which present similar smaller
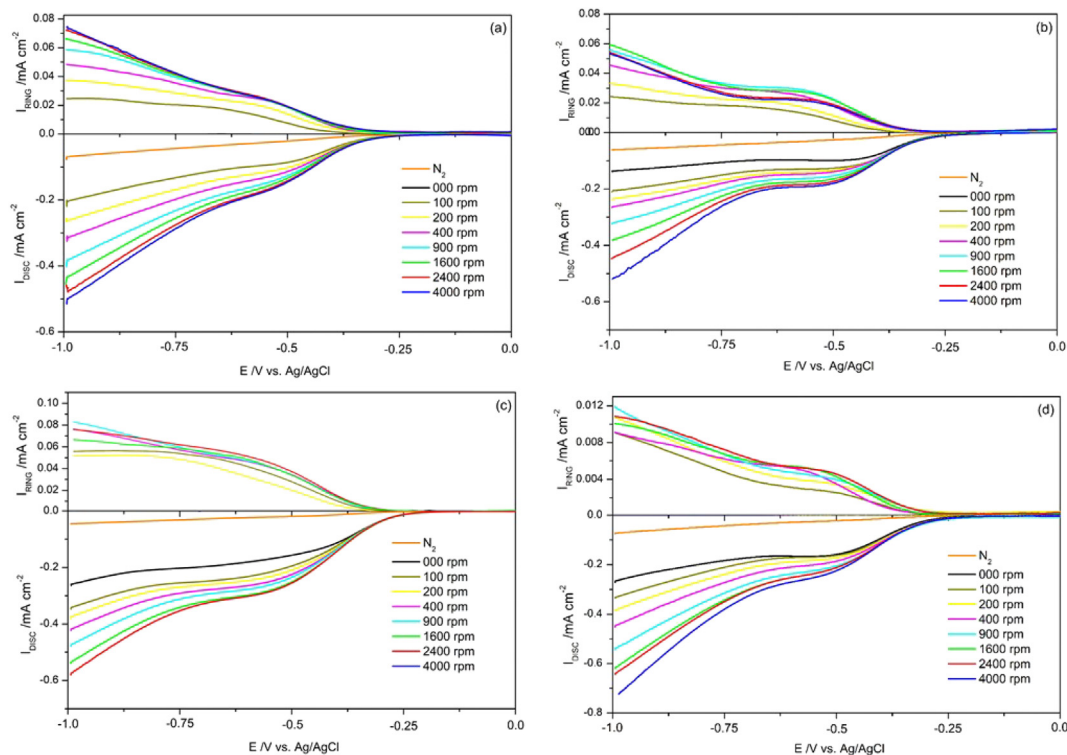
Fig. 4. RRDE LSV curves of the different chromium oxide–carbon composites (b: Cr_2O_3-GO; c: Cr_2O_3-graphene; d: Cr_2O_3-graphite), as well as those obtained from the nanoparticles without carbon allotropes (a). Scan rate v = 0.05 Vs^{-1} in air and N_2 saturated 0.1 KOH electrolyte. The values of the rotation rates (in rpm) are given in the curves.

onset potentials (0.65 ± 0.2 V vs. RHE) and plateau currents which practically doubles that obtained for Cr_2O_3-GO. In the case of Cr_2O_3 nanoparticles, no clear plateaus are obtained, but the currents are similar to those obtained for Cr_2O_3-GO. Concerning the onset potential corresponding to a current density of -0.1 $mAcm^{-2}$, there is an increase of around 60 mV between the response of the Cr_2O_3-graphene and graphite composites and those of Cr_2O_3 nanoparticles. Both effects (lower onset and higher current plateau) points to a more effective catalytic oxygen conversion in the case of the graphene and graphite modified electrodes. Besides, catalytic activity of pristine graphite and graphene materials have been compared with their Cr_2O_3-based materials (Figure S1 and S2), confirming the improvement of the catalysts when Cr_2O_3 nanoparticles were incorporated into carbonaceous materials.

In order to analyse the electrochemical performance of the ORR chromium-carbon electrocatalysts, the usual approach is to use the RDE or RRDE. Thus, the kinetics of ORR was analysed according to the Koutecky-Levich (KL) expression deduced in the Appendix. KL analysis allows us to obtain overall kinetic parameters for the ORR reaction but it should be taken into account that KL does not provide information relative to the mechanistic pathways of the process. KL implicit assumptions (first order reaction kinetics and a single rate limiting step) restrict its applicability since multistep processes with formation of intermediate products are likely to occur [43]. Nevertheless, it is still a powerful tool in the analysis of kinetic capabilities of ORR catalysts when there is a rate limiting step acting as a bottleneck for the overall process [44,45]. Thus, the validity of KL assumptions can be tested from the experimental results (see below) [46].

In the model developed here, it has been assumed that the rate-limiting step is the electrosorption of the solution soluble oxygen to a given active site in the modified electrode. Under these conditions, the KL expression can be written as (see Appendix),

$$\frac{1}{J_{ss}} = \frac{1}{nFk_{ads}c_{O_2}^*} + \frac{\omega^{-1/2}}{0.62nFc_{O_2}^*\nu^{-1/6}D_{O_2}^{2/3}} \tag{1}$$

where n is the electron transfer number, F is the Faraday constant, $D_{O_2} = 1.93 \times 10^{-5}$ cm^2 s^{-1} is the diffusion coefficient of O_2 in the electrolyte, $\nu = 1.09 \times 10^{-2}$ cm^2 s^{-1} is the kinematic viscosity, and $c_{O_2}^* = 0.256 \times 10^{-6}$ mol cm^{-3} is the bulk concentration of O_2 in the electrolyte using air instead of pure O_2 [47].

Figs. 5 and S3-6 show clear linear dependences of the inverse of the current density on the inverse of the square root of the rotation rate. From the slopes of the linear plots and by applying Equation (1) we have obtained the values of the number of transferred electrons given in this figure. Thus, for Cr_2O_3-Graphene Oxide (Figure S5) and Cr_2O_3 nanoparticles (Figure S6), the values of n are between 1.6 and 2.3 whereas for Cr_2O_3-Graphene (Figure S4) and Cr_2O_3-graphite (Figure S3) the average values are between 2.7 and 3.8, in line with the current–potential curves of Fig. 4. However, it has to be taken in account that the KL theory was originally developed to measure physical quantities, such as the diffusion coefficient of a solute, using certain electrochemical reactions (n was considered as a constant). However, n is not constant during ORR process measured by the RRDE method.

In agreement with the model developed in the Appendix, the adsorption rate constant should depend on the potential in a Butler-Volmer way (see Equation), $k_{ads} = k^0 e^{-\alpha'\eta}$. Therefore, in agreement with Eq. (A.6), a linear dependence between the inverse of the current density and $\omega^{-1/2}$ should be expected, with an intercept logarithm-dependent on the applied potential. Fig. 6 shows the linear dependence between KL plot slopes and ln(intercepts) with E values for all composites and Cr_2O_3 nanoparticles analysed. Although very approximate, from these plots it can be seen an almost identical linear dependence for Cr_2O_3 nanoparticles and Cr_2O_3-graphene oxide, with both of them located a higher $ln(intercept_{KL})$ values. This fact seems to
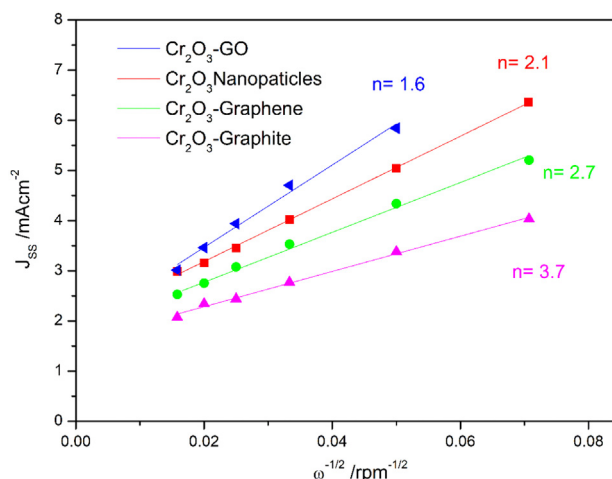
Fig. 5. KL plots for the different chromium oxide–carbon composites as well as that obtained from the nanoparticles without carbon allotropes. Only KL plots at −0.9 V are displayed here, with the n value obtained at this potential. The complete KL plots at different potentials are included in the supplementary information file (Figs. S3–S6).
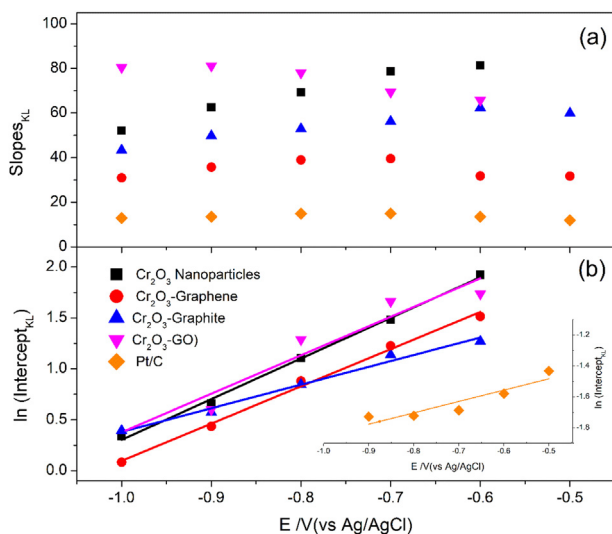

Fig. 6. Dependence of the slope (a) and ln(intercept) (b) values from the KL plot versus potential values, for Cr_2O_3-based composites and Cr_2O_3 nanoparticles. Results obtained for Pt/C have also been included.

indicate a higher activation requirement for these composites, contrarily to Cr_2O_3-graphene and graphite that present lower ln(intercept$_{KL}$) values (Fig. 6.b). Besides, no significant deviations with potential are observed for the KL slopes of graphene and graphite composites, as can be seen in Fig. 6.a. These results agree with our proposed theoretical model, confirming the electrosorption of O_2 molecules at the active sites of the composites as the rate-determining step. However, the KL slopes of Cr_2O_3 nanoparticles and GO composite vary with the potential, confirming a more complex catalyst mechanism. To confirm the application of this model, results obtained for Pt/C have been included as well. Once again, data obtained from KL plot for Pt/C catalyst, demonstrate a dependence of the ln(intercept$_{KL}$) and independence of slopes versus potential values.

The inconsistencies arisen from KL method when obtaining the electron transfer number point towards the non-compliance of the KL assumptions in the case of Cr_2O_3-graphene oxide and Cr_2O_3 nanoparticles and suggest that a more complex pathway should be

considered in these cases. In order to gain further insight into the reaction kinetics, RRDE tests were also analysed by using Eqs. (2) and (3) relative to the dependence of the electron transfer number and the percentage ratio of HO_2^- on the electrode potential[46]

$$n = \frac{4I_d}{I_d + \left(\frac{I_r}{N}\right)} \quad (2)$$

$$\%HO_2^- = 200\frac{I_r/N}{I_d + \left(\frac{I_r}{N}\right)} \quad (3)$$

where I_d is the disk current, I_r is the ring current, and N is the geometric factor of the RRDE, more often denoted as the current collection efficiency of the Pt ring, which was determined to be 42.4 [48,49]. The results obtained for the four modified electrodes at 1600 rpm in the potential range (−1.0, −0.6) V are shown in Fig. 7. Besides, Figure S7-S10 display de n and $\%HO_2^-$ values for all electrodes and rotating rates. As can be seen, only the graphite composite shows a n value close to 4 (3.7–3.9), in agreement with the value obtained for KL treatment. However, graphene and GO composites as well as Cr_2O_3 nanoparticles reported n values ranging between 2.5 and 3. This result points to a higher catalytic activity for the Cr_2O_3-graphite composite. Note that only the n values obtained for graphene and graphite composites agree with those derived from KL method, confirming a higher consistency of the KL treatment in these cases. Nevertheless, KL limitations should be taken into account when complex kinetic processes are analysed, as indicated by different authors [50,51].

Fig. 7 also shows that the percentage of HO_2^- for graphite composite slightly increase with the decrease of electrode potential, but maintaining always significantly lower values, ranging between 4 and 11%,
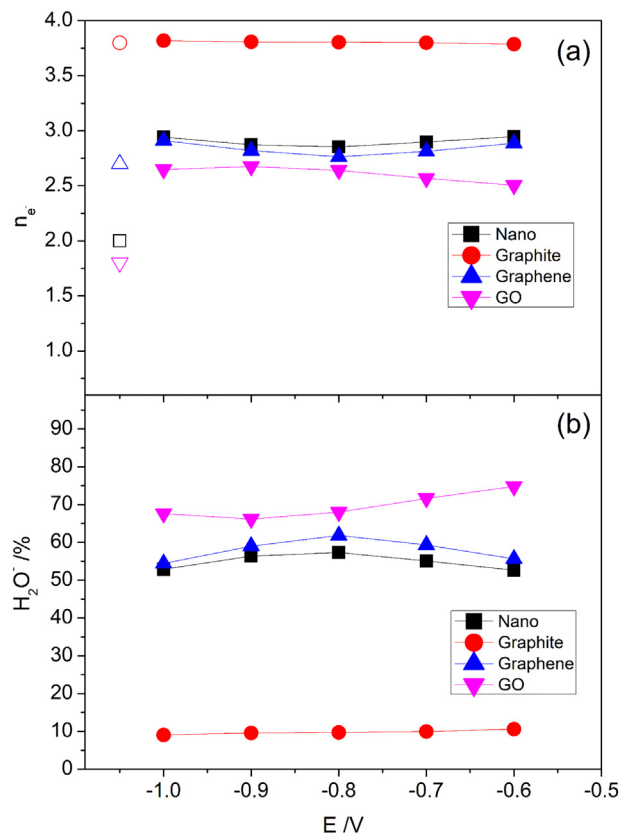

Fig. 7. Dependence of the electron transfer number and the percentage ratio of HO_2^- on the electrode potential calculated from Equations (2) and (3) from the data in Fig. 5. The data correspond to Cr_2O_3-graphene oxide, Cr_2O_3-graphite, Cr_2O_3-graphene, as well as those obtained from the nanoparticles without carbon allotropes. Rotation rate: 1600 rpm.
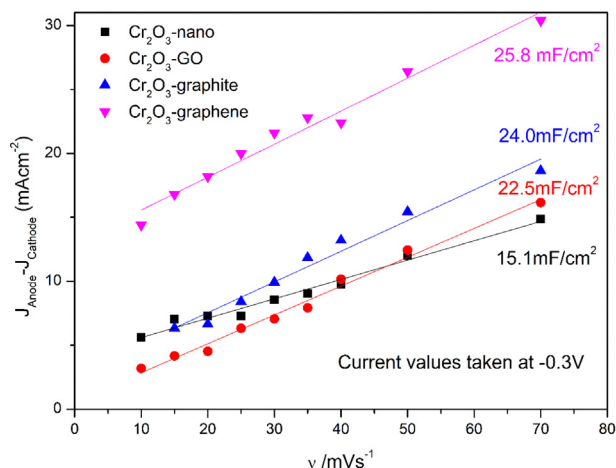
Fig. 8. Plots of the difference of anodic and cathodic current densities against the scan rate for the Cr_2O_3 composites and Cr_2O_3 nanoparticles.

Fig. 9. LSV curves obtained before and after 1600 voltammetric cycles for Cr_2O_3-Graphene (a) and Cr_2O_3-Graphite (b) materials.

than those obtained for Cr_2O_3 nanoparticles, as well as graphene and GO composites. This result confirms that the ORR occurred almost exclusively by a 4 e$^-$ mechanism. However, the percentage of HO_2^- for graphene and GO composites as well as Cr_2O_3 nanoparticles are always higher than 50%, indicating a mixed contribution of a different ORR mechanistic pathways, an evidence also supported by the KL results. The higher catalytic activity of the Cr_2O_3-graphite composite may be explained by the strong interaction revealed by Raman spectroscopy between Cr_2O_3 nanoparticles and graphite (see Raman section). This interaction provides a synergistic effect enhancing the catalytic properties of Cr_2O_3-graphite composite, which is not observed for GO and graphene composites.

With the aim of estimating the amount of active sites for the ORR catalyst we have adapted a method proposed by M.B. Stevens et al. applied to OER[52,53]. We have carried out a voltammetric study of the composites in a capacitive region, -0.3 to -0.1 V, where there is no faradaic contribution. Fig. 8 shows the differences of anodic and cathodic current densities versus scan rates[52–54], obtaining slopes (areal capacitance) proportional to the number of active sites as well as to the electrochemical surface area of each sample. As can be seen, graphene and graphite composites report the higher areal capacitances, 25.8 and 24.0 mF cm^{-2}, whereas Cr_2O_3 nanoparticles reached only 15.0 mF cm^{-2}. This result agrees with the smaller ORR
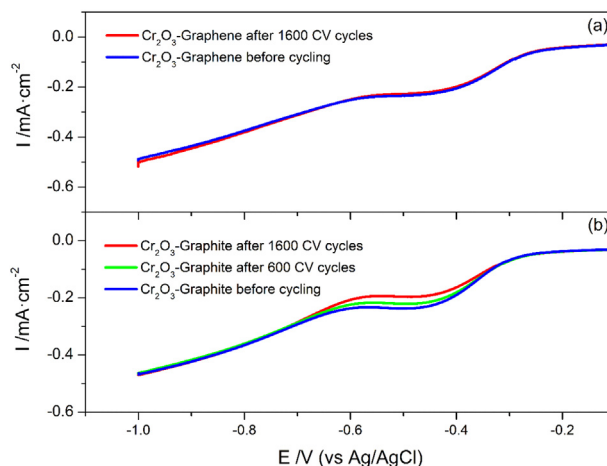
onset and higher n values obtained for Cr_2O_3-graphene and Cr_2O_3-graphite composites, confirming that these materials enable abundant active sites to promote the eletrocataliytic activity of the Cr_2O_3.

Moreover, long term analyses of Cr_2O_3-Graphene and Cr_2O_3-Graphite materials have been carried out to test the stability of the Cr_2O_3-based materials with the cycling. As shown in Fig. 9, the agreement of LSV curves obtained before and after 1600 CV cycles is extraordinary for the graphene-based material. As regards to Cr_2O_3-Graphite, a very good stability is also obtained, although a minimal intensity decreasing is observed only in the -0.3 V to -0.7 V range. These results confirm the high stability with the cycling of both materials.

Finally, catalyst properties of the Cr_2O_3-graphite composites have been tested as cathode electrode in a Zn/PVA-KOH/air battery, demonstrating its applicability as ORR catalyst in a real metal/air battery. Specific capacities of 195 and 266 mAhg^{-1} were obtained using Cr_2O_3-graphite-based electrodes with 9 wt% and 25 wt%, respectively. As can be seen, a much lower capacity of 132 mAhg^{-1} was achieved for Cr_2O_3 nanoparticles 25 wt%-based electrode (Fig. 10.a). Moreover, a polarization study has been carried out for the Zn/PVA-KOH/air battery using a Cr_2O_3-graphite-based electrode. Fig. 10.b shows the potential and power values versus current intensity, resulting specific power value maximum of 0.41 kW·kg^{-1} at discharge current of 75 mA cm^{-2}.
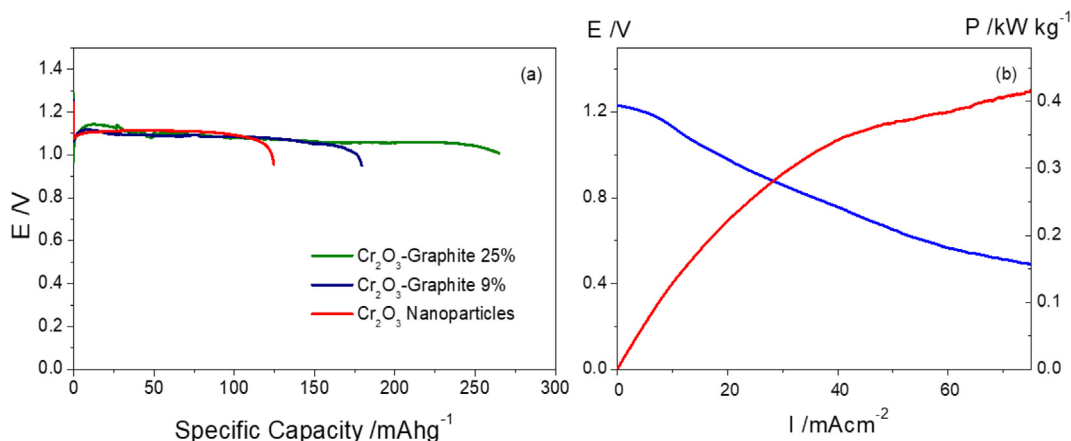

Fig. 10. a) Discharge curves of Zn/PVA-KOH/air batteries using cathodes with different catalyst: Cr_2O_3 nanoparticles 25 wt% and Cr_2O_3-graphite at 9 and 25 wt %. b) Potential and specific Power versus Current Intensity obtained during polarization measurements of a Zn/PVA-KOH battery using a 25% wt Cr_2O_3-graphite-based cathode. Specific capacity and power values were calculated with the total mass of cathode and anode electrodes.

4. Conclusions.

In this work, highly crystalline Cr_2O_3 nanoparticles and their composites with graphite, graphene and GO have been synthesized by a soft chemistry route which preserves the structure and properties of the carbon material while yielding phase pure, highly crystalline oxide nanostructures, as evidenced by XRD, HRTEM and micro-Raman spectroscopy. The obtained materials have been examined as catalyst for the oxygen reduction reaction by different electrochemical methods. A reduction mechanism assuming that the rate limiting step of the process is the electrosorption of oxygen has been proposed. The results obtained by Koutecky-Levich analysis indicates that the behaviours of graphene and graphite composites are consistent with the model proposed, showing ln(intercept$_{KL}$) linear dependence, but slopes$_{KL}$ independence vs. potential values. Moreover, these composites show the lower onset and the higher intensities as well as superior numbers of active sites and good stabilities in long term analyses. However, the catalytic performance of Cr_2O_3 nanoparticles and the Cr_2O_3-GO composite point towards a different reaction pathway for the ORR. Besides, Cr_2O_3-graphite provided an electron transfer number close to 4 electrons for the O_2 reduction, indicating a direct conversion of O_2 to OH^-. This behaviour can be related to the high amount of active sites for the catalyst process found for Cr_2O_3-graphene and Cr_2O_3-graphite, as compared to Cr_2O_3 nanoparticles. However, the strong interaction revealed by Raman spectroscopy between Cr_2O_3 nanoparticles and graphite gives rise to a synergistic effect which enhances the catalytic performance of the Cr_2O_3-graphite composite.

CRediT authorship contribution statement

Paloma Almodóvar: Investigation. **Florencio Santos:** Conceptualization, Investigation, Writing - original draft. **Joaquín Gonzalez:** Conceptualization, Methodology, Writing - original draft, Writing - review & editing. **Julio Ramírez-Castellanos:** Investigation, Resources. **José María González-Calbet:** Resources, Methodology. **Carlos Díaz-Guerra:** Resources, Methodology, Writing - review & editing, Supervision. **Antonio J. Fernández Romero:** Conceptualization, Writing - review & editing, Visualization, Supervision.

Declaration of Competing Interest

The authors declare that they have no known competing financial interests or personal relationships that could have appeared to influence the work reported in this paper.

Acknowledgements

Appendix

The process under study corresponds to the oxygen reduction reaction (ORR) at a glassy carbon electrode modified with chromium oxide nanoparticles with different carbon allotropes. We will assume that the rate limiting step of the process is the electrosorption of oxygen in solution to give a charged surface state leading to superoxo or oxo oxygen confined moieties depending on the potential region (step (1)) [55,56],

$$
\left. \begin{aligned}
O_2)_{sol} + ne^- \ &\underset{k_{ox}}{\overset{k_{red}}{\rightleftarrows}}\ O_2^{n-})_{surf} \ (1)\\
O_2^{n-})_{surf} &\rightarrow HO_2^- \ (2a)\\
O_2^{n-})_{surf} &\rightarrow HO^- \ (2b)
\end{aligned} \right\} \quad (I)
$$

The electrosorption of oxygen will be considered as the rate limiting step of the overall process. These surface confined reduced oxygen states evolves in further subsequent steps in order to release peroxo or hydroxo species in the electrolytic medium (steps (2a) or (2b)). Under these conditions, the apparent kinetics of the overall process leads to a current expression in the way

$$
\frac{I}{nFA} = k_{ad}c_{O_2}^s - k_{des}\Gamma_{O_2^{n-}} \tag{A.1}
$$

with $c_{O_2}^s$ being the surface concentration of oxygen in solution at the nanoparticle-solution interface and $\Gamma_{O_2^{n-}}$ the surface excess of electrosorped oxygen charged species.

It will be assumed that the dependence on potential of the electrosorption and electro-desorption rate constants is given by a Butler-Volmer type formalism [57],

$$
\left. \begin{aligned}
k_{ads} &= k^0 e^{-\alpha\gamma\eta} = k^0 e^{-\alpha'\eta}\\
k_{des} &= k^0 e^{(1-\alpha)\gamma\eta} = k^0 e^{(1-\alpha)'\eta}
\end{aligned} \right\} \tag{A.2}
$$

with γ being the electrosorption valence, which is a function of the applied potential, and

$$
\eta = \frac{nF}{RT}\left(E - E_{ads}^{0'}\right) \tag{A.3}
$$

where $E_{ads}^{0'}$ is the equilibrium potential for the electro-sorption/electro-desorption process [57]. Equations (A.2) indicate that the equivalent cathodic and anodic "charge transfer coefficients" for the electro-sorption and electro-desorption processes have apparent values since $\alpha' = \alpha\gamma$ and $(1-\alpha)' = (1-\alpha)\gamma$. Indeed, $\alpha'n$ is the only magnitude that can be obtained from a Tafel analysis of the foot of the cathodic wave.

The flux of oxygen to the nanoparticles surface is directly related to the electrosorption process (if we consider a fully irreversible character), that is,

$$
D_{O_2}\left(\frac{dc_{O_2}}{dx}\right)_{x=0} = k_{ad}c_{O_2}^s \tag{A.4}
$$

We will assume a stationary mass transport condition for oxygen since a rotating disc electrode is causing a convective transport of O_2 towards the electrode surface. Under these conditions, the concentration profile of O_2 can be obtained by solving the following equation [58]:

$$
\frac{d^2c_{O_2}}{dx^2} = -\frac{x^2}{B}\frac{dc_{O_2}}{dx} \tag{A.5}
$$

where,

$$
B = \frac{D_{O_2}}{0.51\omega^{3/2}\nu^{-1/2}} \tag{A.6}
$$

D_{O_2} is the diffusion coefficient of oxygen, ω is the rotation speed of the RDE and ν is the kinetic viscosity of the solvent. By solving Eq. (A.5) the following expression for the surface concentration of species O_2 is obtained

$$
c_{O_2}^s = c_{O_2}^* - 1.29B^{1/3}\left(\frac{dc_{O_2}}{dx}\right)_{x=0} \tag{A.7}
$$

By inserting Eqs. (A.7) into (A.4) and solving for $c_{O_2}^s$ it is obtained

$$
c_{O_2}^s = \frac{c_{O_2}^*}{1 + \frac{1.29B^{1/3}k_{ad}}{D_{O_2}}} \tag{A.8}
$$

Koutecky-Levich analysis

This type of analysis is carried out under stationary conditions. Typically, the inverse of the current density is divided into two contributions related to a redox kinetics contribution and a mass transport contribution[43,45] . In this case, we have assumed that the activation term is related to the electrosorption of molecular oxygen to the nanoparticle surface. Thus, from Eq. (A.1) under fully irreversible redox conditions, by solving for the inverse of the current density we obtain

$$\frac{1}{J_{ss}} = \frac{1}{nFk_{ads}c^*_{O_2}} + \frac{1.29B^{1/3}}{nFc^*_{O_2}D_{O_2}} = \frac{1}{nFk_{ads}c^*_{O_2}} + \frac{\omega^{-1/2}}{0.62nFc^*_{O_2}\nu^{-1/6}D^{2/3}_{O_2}} \qquad (A.9)$$

where J_{ss} is the steady state current density (in A cm^{-2}) and ω is the rotation speed in rad s^{-1}. In agreement with the above equation, the plot of J_{ss}^{-1} vs. $\omega^{-1/2}$ should be linear.

By inserting the values of D_{O_2}, $c_{O_2}*$ and ν, Eq. (A.9) becomes

$$J_{ss}^{-1}\left(\text{mA cm}^{-2}\right) = \frac{40.5 \times 10^{-3}}{nk_{ads}} + \frac{132.06}{n}\omega^{-1/2}\left(\text{rpm}^{-1/2}\right) \qquad (A.10)$$

In agreement with Eqs. (A.2) and (A.9), the slope of these plots should be independent on the applied potential whereas the logarithm of the intercepts should show a linear dependence with the applied potential since,

$$\ln(\text{intercept}) = -\ln\left(nFk^0c^*_{O_2}\right) + \frac{\alpha\gamma nF}{RT}\left(E - E^{0'}_{ads}\right) \qquad (A.11)$$

Appendix A. Supplementary data

Supplementary data to this article can be found online at https://doi.org/10.1016/j.jelechem.2021.115441.

References

[1] F. Si, Y. Zhang, L. Yan, J. Zhu, M. Xiao, C. Liu, et al, Electrochemical Oxygen Reduction Reaction, Elsevier B.V. (2014), https://doi.org/10.1016/B978-0-444-63278-4.00004-5.

[2] M. Keersemaker, Critical Raw Materials (2020) 69–82, https://doi.org/10.1007/978-3-030-40268-6_9.

[3] D. Wu, X. Shen, Y. Pan, L. Yao, Z. Peng, Platinum Alloy Catalysts for Oxygen Reduction Reaction: Advances, Challenges and Perspectives. ChemNanoMat 6 (1) (2020) 32–41, https://doi.org/10.1002/cnma.v6.110.1002/cnma.201900319.

[4] Wang C, Markovic NM, Stamenkovic VR. Advanced Platinum Alloy Electrocatalysts for the Oxygen Reduction Reaction 2012.

[5] K. Chen, Y. Hao, M. Zhang, D. Zhou, Y. Cao, Y. Wang, L. Feng, Nitrogen, sulfur and phosphorus-codoped carbon with a tunable nanostructure as an efficient electrocatalyst for the oxygen reduction reaction, RSC Advances 7 (10) (2017) 5782–5789, https://doi.org/10.1039/C6RA21540H.

[6] C. Yang, S. Tao, N. Huang, X. Zhang, J. Duan, R. Makiura, S. Maenosono, Heteroatom-Doped Carbon Electrocatalysts Derived from Nanoporous Two-Dimensional Covalent Organic Frameworks for Oxygen Reduction and Hydrogen Evolution, ACS Applied Nano Materials 3 (6) (2020) 5481–5488, https://doi.org/10.1021/acsanm.0c0078610.1021/acsanm.0c00786.s001.

[7] X. Yan, Y.i. Jia, X. Yao, Defects on carbons for electrocatalytic oxygen reduction, Chemical Society Reviews 47 (20) (2018) 7628–7658, https://doi.org/10.1039/C7CS00690J.

[8] X. Jin, Y. Xie, J. Huang, Highly effective dual transition metal macrocycle based electrocatalyst with macro-/mesoporous structures for oxygen reduction reaction, Catalysts 7 (7) (2017) 201, https://doi.org/10.3390/catal7070201.

[9] A. Kumar, Y. Zhang, W. Liu, X. Sun, The chemistry, recent advancements and activity descriptors for macrocycles based electrocatalysts in oxygen reduction reaction, Coordination Chemistry Reviews 402 (2020) 213047, https://doi.org/10.1016/j.ccr.2019.213047.

[10] Gong K, Du F, Xia Z, Durstock M, Dai L. Nitrogen-Doped Carbon Nanotube Arrays with High Electrocatalytic Activity for Oxygen Reduction. Science 2009;323:760 LP – 764. https://doi.org/10.1126/science.1168049.

[11] L.M. Rivera, G. García, E. Pastor, Novel graphene materials for the oxygen reduction reaction, Current Opinion in Electrochemistry 9 (2018) 233–239, https://doi.org/10.1016/j.coelec.2018.05.009.

[12] M.A. Molina-García, N.V. Rees, "Metal-free" electrocatalysis: Quaternary-doped graphene and the alkaline oxygen reduction reaction, Applied Catalysis A: General 553 (2018) 107–116, https://doi.org/10.1016/j.apcata.2017.12.014.

[13] D. Higgins, P. Zamani, A. Yu, Z. Chen, The application of graphene and its composites in oxygen reduction electrocatalysis: a perspective and review of recent progress, Energy Environ Sci 9 (2) (2016) 357–390, https://doi.org/10.1039/C5EE02474A.

[14] J. Zhang, Z. Xia, L. Dai, Carbon-based electrocatalysts for advanced energy conversion and storage, Sci Adv 1 (7) (2015) e1500564, https://doi.org/10.1126/sciadv.1500564.

[15] S. Liu, G. Li, Y. Gao, Z. Xiao, J. Zhang, Q. Wang, X. Zhang, L.i. Wang, Doping carbon nanotubes with N, S, and B for electrocatalytic oxygen reduction: A systematic investigation on single, double, and triple doped modes, Catalysis Science and Technology 7 (18) (2017) 4007–4016, https://doi.org/10.1039/C7CY00491E.

[16] Y. Zheng, Y. Jiao, L. Ge, M. Jaroniec, S.Z. Qiao, Two-step boron and nitrogen doping in graphene for enhanced synergistic catalysis, Angewandte Chemie - International Edition 52 (11) (2013) 3110–3116, https://doi.org/10.1002/anie.201209548.

[17] J. Zhang, J. Wang, Z. Wu, S. Wang, Y. Wu, X. Liu, Heteroatom (nitrogen/sulfur)-doped graphene as an efficient electrocatalyst for oxygen reduction and evolution reactions, Catalysts 8 (2018) 19–22, https://doi.org/10.3390/catal8100475.

[18] S. Bag, B. Mondal, A.K. Das, C.R. Raj, Nitrogen and sulfur dual-doped reduced graphene oxide: Synergistic effect of dopants towards oxygen reduction reaction, Electrochimica Acta 163 (2015) 16–23, https://doi.org/10.1016/j.electacta.2015.02.130.

[19] R. Ma, G. Lin, Y. Zhou, Q. Liu, T. Zhang, G. Shan, M. Yang, J. Wang, A review of oxygen reduction mechanisms for metal-free carbon-based electrocatalysts, Npj Computational Materials 5 (1) (2019), https://doi.org/10.1038/s41524-019-0210-3.

[20] Y. Xue, S. Sun, Q. Wang, Z. Dong, Z. Liu, Transition metal oxide-based oxygen reduction reaction electrocatalysts for energy conversion systems with aqueous electrolytes, Journal of Materials Chemistry A 6 (23) (2018) 10595–10626, https://doi.org/10.1039/C7TA10569J.

[21] Y. Wang, J. Li, Z. Wei, Transition-metal-oxide-based catalysts for the oxygen reduction reaction, Journal of Materials Chemistry A 6 (18) (2018) 8194–8209, https://doi.org/10.1039/C8TA01321G.

[22] X. Huang, T. Shen, T. Zhang, H. Qiu, X. Gu, Z. Ali, Y. Hou, Efficient Oxygen Reduction Catalysts of Porous Carbon Nanostructures Decorated with Transition Metal Species, Advanced Energy Materials 10 (11) (2020) 1900375, https://doi.org/10.1002/aenm.v10.1110.1002/aenm.201900375.

[23] C. Goswami, K.K. Hazarika, P. Bharali, Transition metal oxide nanocatalysts for oxygen reduction reaction, Materials Science for Energy Technologies 1 (2) (2018) 117–128, https://doi.org/10.1016/j.mset.2018.06.005.

[24] S.Z. Hussain, M. Ihrar, S.B. Hussain, W.C. Oh, K. Ullah, A review on graphene based transition metal oxide composites and its application towards supercapacitor electrodes, SN Applied Sciences 2 (2020) 1–23, https://doi.org/10.1007/s42452-020-2515-8.

[25] C. Wen, X. Gao, T. Huang, X. Wu, L. Xu, J. Yu, H. Zhang, Z. Zhang, J. Han, H. Ren, Reduced graphene oxide supported chromium oxide hybrid as high efficient catalyst for oxygen reduction reaction, International Journal of Hydrogen Energy 41 (26) (2016) 11099–11107, https://doi.org/10.1016/j.ijhydene.2016.05.051.

[26] F. Santos, A. Urbina, J. Abad, R. López, C. Toledo, A.J. Fernández Romero, Environmental and economical assessment for a sustainable Zn/air battery, Chemosphere 250 (2020) 126273, https://doi.org/10.1016/j.chemosphere.2020.126273.

[27] J.J. Yang, W.N. Martens, R.L. Frost, Transition of chromium oxyhydroxide nanomaterials to chromium oxide: A hot-stage Raman spectroscopic study, Journal of Raman Spectroscopy 42 (5) (2011) 1142–1146, https://doi.org/10.1002/jrs.2773.

[28] V.S. Jaswal, A.K. Arora, M. Kinger, V.D. Gupta, J. Singh, Synthesis and characterization of chromium oxide nanoparticles, Oriental Journal of Chemistry 30 (2) (2014) 559–566.

[29] W.S. Hummers, R.E. Offeman, Preparation of Graphitic Oxide, Journal of the American Chemical Society 80 (6) (1958) 1339, https://doi.org/10.1021/ja01539a017.

[30] L.P. Lingamdinne, J.R. Koduru, Y.-L. Choi, Y.-Y. Chang, J.-K. Yang, Studies on removal of Pb(II) and Cr(III) using graphene oxide based inverse spinel nickel ferrite nano-composite as sorbent, Hydrometallurgy 165 (2016) 64–72, https://doi.org/10.1016/j.hydromet.2015.11.005.

[31] S. Yang, L. Li, Z. Pei, C. Li, J. Lv, J. Xie, B. Wen, S. Zhang, Adsorption kinetics, isotherms and thermodynamics of Cr(III) on graphene oxide, Colloids and Surfaces A: Physicochemical and Engineering Aspects 457 (2014) 100–106, https://doi.org/10.1016/j.colsurfa.2014.05.062.

[32] F. Santos, J.P. Tafur, J. Abad, A.J. Fernández Romero, Structural modifications and ionic transport of PVA-KOH hydrogels applied in Zn/Air batteries, Journal of Electroanalytical Chemistry 850 (2019) 113380, https://doi.org/10.1016/j.jelechem.2019.113380.

[33] S. Lorca, F. Santos, J. Abad, Y. Huttel, A. Urbina, A.J. Fernández Romero, Sustainable Energy Fuels 4 (2020) 4497–4505, https://doi.org/10.1039/d0se00551g.

[34] A.S.O. Gomes, N. Yaghini, A. Martinelli, E. Ahlberg, A micro-Raman spectroscopic study of Cr(OH)3 and Cr2O3 nanoparticles obtained by the hydrothermal method, Journal of Raman Spectroscopy 48 (10) (2017) 1256–1263, https://doi.org/10.1002/jrs.v48.1010.1002/jrs.5198.

[35] J.J. Yang, H. Cheng, W.N. Martens, R.L. Frost, Transition of synthetic chromium oxide gel to crystalline chromium oxide: a hot-stage Raman spectroscopic study, Journal of Raman Spectroscopy 42 (5) (2011) 1069–1074, https://doi.org/10.1002/jrs.2794.

[36] M.A. Pimenta, G. Dresselhaus, M.S. Dresselhaus, L.G. Cançado, A. Jorio, R. Saito, Studying disorder in graphite-based systems by Raman spectroscopy, Physical

Chemistry Chemical Physics 9 (11) (2007) 1276–1290, https://doi.org/10.1039/B613962K.

[37] A.C. Ferrari, Raman spectroscopy of graphene and graphite: Disorder, electron-phonon coupling, doping and nonadiabatic effects, Solid State Communications 143 (1-2) (2007) 47–57, https://doi.org/10.1016/j.ssc.2007.03.052.

[38] A.C. Ferrari, D.M. Basko, Raman spectroscopy as a versatile tool for studying the properties of graphene, Nature Nanotechnology 8 (4) (2013) 235–246, https://doi.org/10.1038/nnano.2013.46.

[39] Z.H. Ni, H.M. Wang, Y. Ma, J. Kasim, Y.H. Wu, Z.X. Shen, Tunable stress and controlled thickness modification in graphene by annealing, ACS Nano 2 (5) (2008) 1033–1039, https://doi.org/10.1021/nn800031m.

[40] J. Yan, E.A. Henriksen, P. Kim, A. Pinczuk, Observation of anomalous phonon softening in bilayer graphene, Physical Review Letters 101 (2008), https://doi.org/10.1103/PhysRevLett.101.136804 136804.

[41] S. Ryu, L.i. Liu, S. Berciaud, Y.-J. Yu, H. Liu, P. Kim, G.W. Flynn, L.E. Brus, Atmospheric oxygen binding and hole doping in deformed graphene on a SiO2 substrate, Nano Letters 10 (12) (2010) 4944–4951, https://doi.org/10.1021/nl1029607.

[42] S. Cao, Z. Xiao, C.-P. Kwan, K. Zhang, J.P. Bird, L.u. Wang, W.-N. Mei, X. Hong, P. A. Dowben, Moving towards the magnetoelectric graphene transistor, Applied Physics Letters 111 (18) (2017) 182402, https://doi.org/10.1063/1.4999643.

[43] R. Zhou, Y. Zheng, M. Jaroniec, S.-Z. Qiao, Determination of the Electron Transfer Number for the Oxygen Reduction Reaction: From Theory to Experiment, ACS Catalysis 6 (7) (2016) 4720–4728, https://doi.org/10.1021/acscatal.6b0158110.1021/acscatal.6b01581.s001.

[44] V. Di Noto, E. Negro, A. Nale, G. Pagot, K. Vezzù, P. Atanassov, Hidden in plain sight: unlocking the full potential of cyclic voltammetry with the thin-film rotating (ring) disk electrode studies for the investigation of oxygen reduction reaction electrocatalysts. Current Opinion, Electrochemistry 25 (2021) 100626, https://doi.org/10.1016/j.coelec.2020.08.008.

[45] S. Xu, Y. Kim, D. Higgins, M. Yusuf, T.F. Jaramillo, F.B. Prinz, Building upon the Koutecky-Levich Equation for Evaluation of Next-Generation Oxygen Reduction Reaction Catalysts, Electrochimica Acta 255 (2017) 99–108, https://doi.org/10.1016/j.electacta.2017.09.145.

[46] Z. Jia, G. Yin, J. Zhang, Rotating Ring-Disk Electrode Method. Rotating Electrode Methods and Oxygen Reduction Electrocatalysts, Elsevier B.V. (2014) 171–198, https://doi.org/10.1016/B978-0-444-63278-4.00005-7.

[47] W. Xing, M. Yin, Q. Lv, Y. Hu, C. Liu, J. Zhang, Oxygen Solubility, Diffusion Coefficient, and Solution Viscosity. Rotating Electrode Methods and Oxygen Reduction Electrocatalysts, Elsevier B.V. (2014) 1–31, https://doi.org/10.1016/B978-0-444-63278-4.00001-X.

[48] F. Dalton, Historical Origins of the Rotating Ring-Disk Electrode, Interface Magazine 25 (2016) 50–59.

[49] Y. Garsany, J. Ge, J. St-Pierre, R. Rocheleau, K. Swider-Lyons, ORR Measurements Reproducibility Using a RRDE, ECS Transactions 58 (1) (2013) 1233–1241, https://doi.org/10.1149/05801.1233ecst.

[50] H.-J. Zhang, H. Li, X. Li, H. Qiu, X. Yuan, B. Zhao, Z.-F. Ma, J. Yang, Pyrolyzing cobalt diethylenetriamine chelate on carbon (CoDETA/C) as a family of non-precious metal oxygen reduction catalyst, International Journal of Hydrogen Energy 39 (1) (2014) 267–276, https://doi.org/10.1016/j.ijhydene.2013.09.084.

[51] M. Mamlouk, S.M.S. Kumar, P. Gouerec, K. Scott, Electrochemical and fuel cell evaluation of Co based catalyst for oxygen reduction in anion exchange polymer membrane fuel cells, Journal of Power Sources 196 (18) (2011) 7594–7600, https://doi.org/10.1016/j.jpowsour.2011.04.045.

[52] T. Kou, S. Wang, J.L. Hauser, M. Chen, S.R.J. Oliver, Y. Ye, J. Guo, Y. Li, Ni Foam-Supported Fe-Doped β-Ni(OH) 2 Nanosheets Show Ultralow Overpotential for Oxygen Evolution Reaction, ACS Energy Letters 4 (3) (2019) 622–628, https://doi.org/10.1021/acsenergylett.9b0004710.1021/acsenergylett.9b00047.s001.

[53] M.B. Stevens, L.J. Enman, A.S. Batchellor, M.R. Cosby, A.E. Vise, C.D.M. Trang, S. W. Boettcher, Measurement techniques for the study of thin film heterogeneous water oxidation electrocatalysts, Chemistry of Materials 29 (1) (2017) 120–140, https://doi.org/10.1021/acs.chemmater.6b02796.

[54] A. Zuliani, M. Cano, F. Calsolaro, A.R. Puente Santiago, J.J. Giner-Casares, E. Rodríguez-Castellón, G. Berlier, G. Cravotto, K. Martina, R. Luque, Improving the electrocatalytic performance of sustainable Co/carbon materials for the oxygen evolution reaction by ultrasound and microwave assisted synthesis, Sustainable Energy & Fuels 5 (3) (2021) 720–731, https://doi.org/10.1039/D0SE01505A.

[55] J. Meng, H. Lei, X. Li, J. Qi, W. Zhang, R. Cao, Attaching Cobalt Corroles onto Carbon Nanotubes: Verification of Four-Electron Oxygen Reduction by Mononuclear Cobalt Complexes with Significantly Improved Efficiency, ACS Catalysis 9 (5) (2019) 4551–4560, https://doi.org/10.1021/acscatal.9b0021310.1021/acscatal.9b00213.s001.

[56] D. Barrera, M. Florent, M. Kulko, T.J. Bandosz, Ultramicropore-influenced mechanism of oxygen electroreduction on metal-free carbon catalysts, Journal of Materials Chemistry A 7 (47) (2019) 27110–27123, https://doi.org/10.1039/C9TA10850E.

[57] A. Szulborska, A. Baranski, Numerical simulation of kinetically controlled electrosorption processes under cyclic voltammetric conditions, Journal of Electroanalytical Chemistry 377 (1-2) (1994) 23–31, https://doi.org/10.1016/0022-0728(94)03437-0.

[58] A.J. Bard, L.R. Faulkner, Electrochemical Methods: Fundamentals and Applications, 2nd Edition., 2001.